Low-Temperature Multi-Mode Microwave Spectroscopy of Paramagnetic and Rare-Earth Ion Spin Impurities in Single Crystal Calcium Tungstate

Elrina Hartman, Michael E Tobar, Ben T McAllister, Jeremy Bourhill, and Maxim Goryachev
*Quantum Technologies and Dark Matter Labs, Department of Physics, University of Western Australia, 35 Stirling Highway, Crawley, WA 6009, Australia.**

(Dated: April 19, 2024)

We present experimental observations of dilute ion spin ensembles in an undoped low-loss single crystal cylindrical sample of $CaWO_4$ cooled to 30 mK in temperature. Crystal field perturbations were elucidated by constructing a dielectrically loaded microwave cavity resonator from the crystal. The resonator exhibited numerous whispering gallery modes with high Q-factors of up to 3×10^7, equivalent to a low loss tangent of $\sim 3 \times 10^{-8}$. The low-loss allowed precision multi-mode spectroscopy of numerous high Q-factor photon-spin interactions. Measurements between 7 to 22 GHz revealed the presence of Gd^{3+}, Fe^{3+}, and another trace species, inferred to be rare-earth, at concentrations on the order of parts per billion. These findings motivate further exploration of prospective uses of this low-loss dielectric material for applications regarding precision and quantum metrology, as well as tests for beyond standard model physics.

I. INTRODUCTION

Scheelite, or calcium tungstate, ($CaWO_4$) has seen a significant rise in interest for its potential of application in a myriad of contexts from test of fundamental physics, communications, and quantum computing when considered in conjunction with spin ensemble dopants such as Gd^{3+}, Er^{3+}[1–8], Yb^{3+} [9], Nd^{3+} [10] and Pr^{3+}[11–13], with particular interest in utilizing rare-earth ions for quantum information storage and processing, and on-chip sensing[14, 15]. The scintallating dielectric also plays a key role in detection of rare events such as neutrinoless double β-decay [16], radioactive decay of very long-living isotopes [17] and searches for weakly interacting massive particles (WIMPs), a candidate for Dark Matter (DM) [18, 19]. The question of interest is whether or not either or both of these application avenues can be realised in a single crystal architecture at low temperatures, and what effects do the residual impurity spin ensembles display. To that end, this report presents the findings of microwave electron spin resonance (ESR) spectroscopy as per the methods in [20] to identify the paramagnetic residual impurities present in a high-purity $CaWO_4$ sample that was purchased from SurfaceNet.

The manufacturer grew the sample in the ⟨100⟩ orientation such that the a-axis of the crystal unit cell was aligned with the z-axis of the macroscopic cylindrical geometry. Typically, ESR studies investigate the ⟨001⟩ orientation, exploiting the symmetry of the tetragonal unit cell belonging to the space group $I4_1/a$ [21]. We report effective values of crystal field parameters, Landé g factors (g_L), zero field splittings (ZFS) and coupling rates (g), and review discrepancies with literature due to directionality. From the results the impurity ion concentrations were calculated, which were not affected by the directionality.

* 21731429@student.uwa.edu.au
michael.tobar@uwa.edu.au

II. EXPERIMENT SETUP

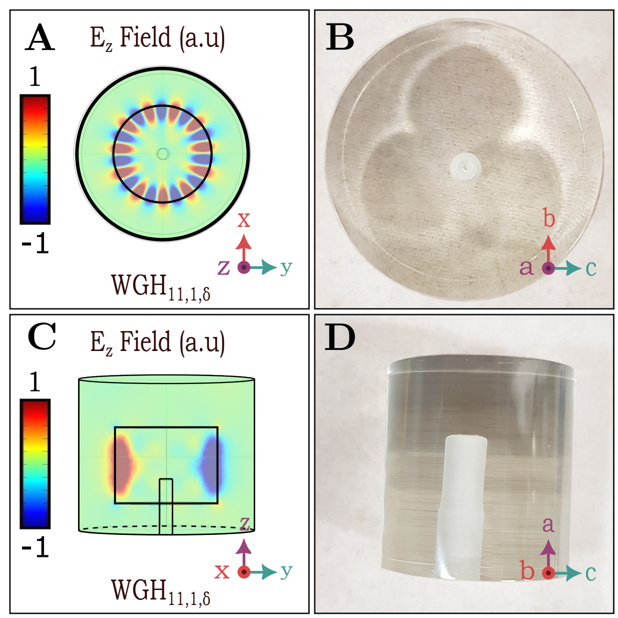

FIG. 1. The $CaWO_4$ crystal purchased from SurfaceNet was grown along the ⟨100⟩ axis so that the c-axis of a unit cell aligns with the radial-axis of the cylinder. The manufacturer drilled a central hole on one side along the z-axis as required for the purpose of mounting the crystal on a post. Here (**A**) and (**C**) shows the schematics of the dielectric resonator, along with the electric-energy density of the E_z field of the quasi-$TM_{11,1,\delta}$ mode (or $WGH_{11,1,\delta}$), calculated using Comsol. Corresponding photographs of the top (**B**) and the side view (**D**) are also shown. The borehole that appears white in the photograph is in a region of low field density for a WGM so frequency perturbations due to the presence of the sapphire post are negligible.

The dielectrically loaded cavity was suspended in a superconducting magnet bore at the 30 mK stage in a dilution refrigerator as shown in Fig. 2. Two straight antenna probes inserted at the base of the cavity to excite high-Q Whispering Gallery Modes (WGM) via microwave coaxial cables connected to room temperature readout using a Vector Network Analyser (VNA). Evanescent fields exist beyond the dielectric surface which decay exponentially in the axial direction above and below the crystal and as a modified Bessel function of the second kind in the radial direction [22]. The probes were inserted to a depth adjusted for under-coupling to these evanescent fields so that the intrinsic losses of the dielectric could be measured. Input power was attenuated at the 4 K and 30 mK stage to reduce thermal noise from the input port. The DC magnetic field, applied along the z-axis of the cylindrical sample (parallel to the a-axis of the crystal unit cell) was then ramped in steps of 1 mT, tuning the spin transition energies across select high-Q WGMs, shown in Fig.3. The ramping rate was set to allow for thermal equilibrium to be reached so as to avoid non-linear effects. The output signal from the cavity passed through an isolator at the 30 mK stage and a cryogenic amplifier at the 4 K stage. A room-temperature amplifier was also used to enhance the signal to noise ratio. Transmission spectra of each mode were recorded at all magnetic field values so the interaction field could be captured, including impacts on the photon mode's frequency, Q-factor, and transmission power.

The associated measurements were specified by the scattering s-parameters S_{21}, forward power gain transfer

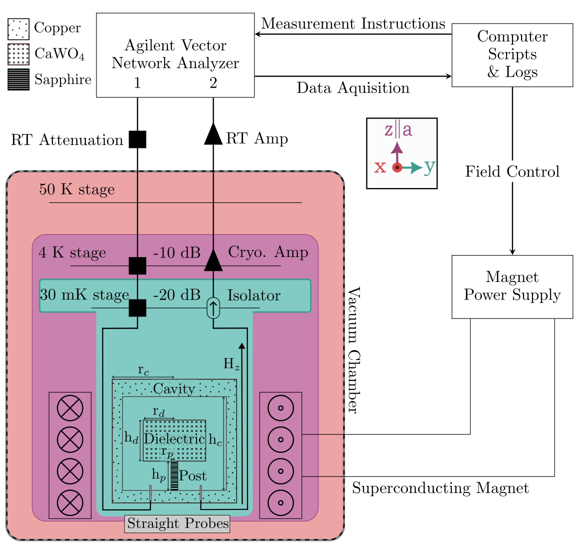

FIG. 2. The $CaWO_4$ dielectric crystal (dim: $r_d = 14.68\,\mathrm{mm}$, $h_d = 20.00\,\mathrm{mm}$) was positioned inside an oxygen-free copper cavity (dim: $r_c = 25.00\,\mathrm{mm}$, $h_c = 40.00\,\mathrm{mm}$), mounted on a sapphire post (dim: $r_p = 1.75\,\mathrm{mm}$, $h_p = 14.50\,\mathrm{mm}$) that slots into a central hole at the base of the crystal and was clamped to the base of the cavity to prevent loss from thermal contact with the cavity's conducting surfaces. A microwave signal was input to the cavity using a Vector Network Analyser (VNA). Control of the VNA and cryogenic dilution refrigerator was automated via computer scripts that set all parameters such as scan rate, power input, magnetic field strength, and frequency span.

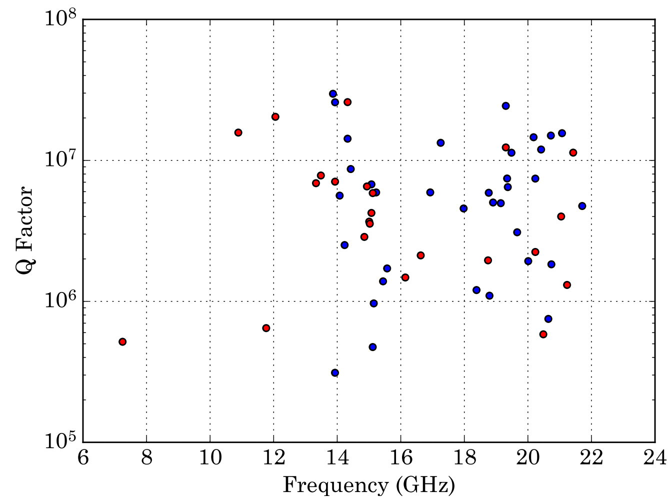

FIG. 3. A large number of high-Q resonances are present in this sample (blue). A spread of resonances were selected (red) in the present study with additional lower-Q modes at lower frequencies to resolve zero field splittings (ZFS).

function, which was measured via the VNA and modelled as a Breit-Wigner distribution or asymmetric Fano pulse, given by [23];

$$|S_{21}| = 1 - \frac{(q\Gamma_p/2 + \Delta)^2}{(\Gamma_p/2)^2 + \Delta^2}\,, \tag{1}$$

where q is the Fano parameter measuring the ratio of resonant scattering to background scattering, Γ_p is the photonic resonance line-width, and Δ is the frequency detuning $(f - f_0)$. The Q-factors of the modes can be calculated from the line-widths and are shown for zero DC magnetic field in Fig. 3. The best Q-factors in the crystal are of order of 3×10^7 close to 14 GHz, indicating a loss tangent of order $\tan\delta \approx 3 \times 10^{-8}$. The exact values of the anisotropic loss components could be verified more precisely using the WGM technique [24–27] in a different sample, which has the cylindrical z-axis aligned with the c-axis in future studies.

III. MULTIMODE SPECTROSCOPY

In order to discern weakly coupled spin systems, we excite spin transitions using high-Q WGMs with the microwave field perpendicular to the DC magnetic field, namely multiple quasi-TM WGMs ranging from 7 to 22 GHz, see Fig. 3. When the energy of a spin transition matches the energy of an injected WGM, the photon microwave resonance and spin resonance couple via a mode interaction, allowing the spin transition to be observed. Results indicate the onset of many avoided level crossings (see the appendix), due to partial hybrization and a perturbation of the microwave mode [28, 29]. The interaction may be modelled as a coupled harmonic oscillator, which manifests as a frequency shift of the microwave mode as well as a sharing of loss mechanisms between the two systems, typically resulting in a transmission amplitude shift and change in the normal mode Q-factor due to losses introduced by the spins [30, 31].

A. Coupling Rate, Spin Linewidths, and Concentration

The photon-spin interactions were modelled as a coupled harmonic oscillator with ω_+ and ω_- as the eigensolutions to the characteristic equation [31–33];

$$\omega_\pm = \frac{1}{\sqrt{2}}\sqrt{\omega_s^2 + \omega_p^2 \pm \sqrt{\omega_s^4 - 2\omega_s^2\omega_p^2 + 4\Delta_{ps}\omega_s^2\omega_p^2 - \omega_p^4}}\,, \tag{2}$$

where ω_p is a particular photonic resonance frequency and ω_s is the spin resonance frequency, and Δ_{ps} is the normalised, unitless, inductive mutual coupling [30] between these two resonant systems. Here, the value of Δ_{ps} parameterises the rate of coupling g ($g := \frac{\Delta_{ps}\omega_p}{2}$). This model ignores loss, so a-priori assumes photon-spin hybridisation in the strong coupling regime, but suffices to fit the perturbation extremely well in the present study due to the fact that the photon linewidths, $\Gamma_p = \frac{\omega_p}{Q_p}$, are of the order kHz, while g is of the order MHz, allowing strong off resonant perturbations of the photon normal modes due to the spins (here Q_p is the mode Q-factor).

In the limit where ω_s is detuned far from ω_p, $\omega_s = \gamma B$ exhibits linear dependence on the magnetic field (H_z) where γ is the gyromagnetic ratio. As ω_s is tuned towards ω_p, the normal modes ω_+ and ω_- are detuned asymptotically around the intersection point, where as in the weak coupling regime, the photonic mode is tuned through the classically forbidden region. When $\omega_s = \omega_p$, the two resonant systems are maximally hybridised, and ω_+ and ω_- represent the normal mode solutions of a coupled system and the rate of coupling the frequency separation of these two modes ($\omega_+ - \omega_- = \Delta_{ps}\omega_p = 2g$), can be extracted by fitting equation 2 to the frequencies of the mode interaction, even in the weak coupling regime because of the high-Q of the microwave modes. With a single photonic resonance, multiple spin interactions can be observed as the magnetic field tunes the latter over the former. Density plots of many of these mode interactions have been included in the appendix.

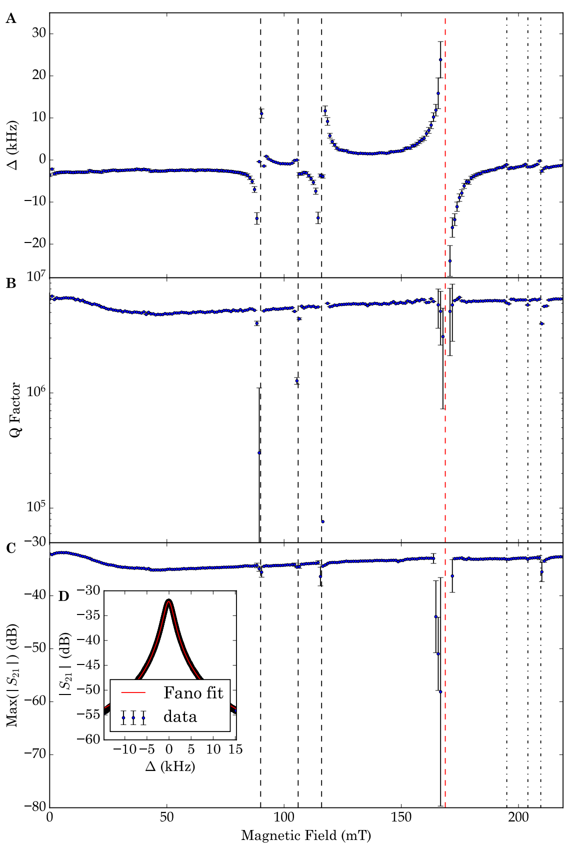

FIG. 4. **A** shows the frequency detuning (Δ) for a selected WGM of frequency $f_0 = 14.934048$ GHz, induced by impurity spins as a function of the applied DC magnetic field. The vertical lines mark the magnetic field positions of the WGM-spin interactions. A large proportion of the identified mode interactions occurred close together and exhibited a range of couplings, from very weak couplings (such as the three dot-dashed lines on the right) to stronger couplings, which in some cases exhibit the onset of an avoided level crossing (i.e. the red, dashed line). The coupling of this strongest interaction was calculated by fitting to the normal-mode frequencies, $\omega_\pm$ to Eq. (2), with a close up shown in Fig. 5. For each mode interaction in **A** there is a corresponding Q-factor degradation shown in **B** (fitted using Eq, (3), and increase in absorption shown (**C**) due to the coupling of magnetic losses. Inset **D** shows an example of the transfer function of the photonic resonance as measured by the VNA, in which the data is extracted of a single point for figures **A**, **B**, and **C**.

The Q-factor of the coupled photon-spin system can be modelled with the following equation [30, 31]:

$$\begin{pmatrix} \frac{\omega_+}{Q_+} \\ \frac{\omega_-}{Q_-} \end{pmatrix} = \begin{pmatrix} 1 & 1 \\ \omega_-^2 & \omega_+^2 \end{pmatrix}^{-1} \begin{pmatrix} 1 & 1 \\ \omega_s^2 & \omega_p^2 \end{pmatrix} \begin{pmatrix} \frac{\omega_p}{Q_p} \\ \frac{\omega_s}{Q_s} \end{pmatrix}. \tag{3}$$

This expression allows for the determination of spin resonance linewidths ($\Gamma_s = \frac{\omega_s}{Q_s}$) and spin quality-factor (Q_s). Fig. 4**B** shows how the Q of the hybrid system in the coupling regime is limited by the highest loss system, which in this case is the spin resonance, leading to the degradation of the photonic resonance quality factor (Q_p). There is a corresponding dip in transmission, demonstrated by Fig. 4**C**. The impurity spin concentration (n) may be derived from the rate of coupling, using the following expression;

$$g = g_L\mu_B\sqrt{\frac{\mu_0\omega_p n\xi_\perp}{4\hbar}}\,, \tag{4}$$

where μ_B is the Bohr Magneton, $\hbar$ is the reduced Planck's constant, $\xi_\perp$ is the perpendicular magnetic filling factor [33] ($\xi_\perp \approx 1$ for TM-WGMs), and μ_0 is the permeability

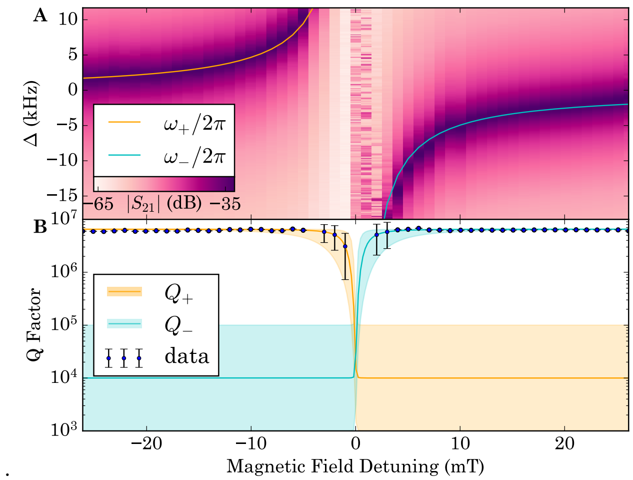

FIG. 5. Close up of the onset of an avoided level crossing between a Gd^{3+} impurity ion transition (identified in the following sub-section), and the 14.934048 GHz WGM at 169 mT, shown in Fig. 4. A) The top figure shows the density plot of the mode interaction, with the fit from Eq. (2) overlayed showing the frequency respones, while, B) the bottom figure shows the fit from Eq. (3) of the Q-factors, which determines the loss in the couple mode system. From the fits the parameters of the mode interaction are given in Tab. I. Note when the spin and photon frequency are equal the system becomes noisey, this is due to the fact that the magnet is not operated in persistent mode. To determine the spin linewidth more precisely from this interaction, a wider span should be taken with a magnet that has persistent mode. However, this was not the focus of this work.

Q_p	Q_s	$\Gamma_p/2$ (kHz)	$\Gamma_s/2$ (MHz)	n $\times 10^{13}$ (cm^{-3})	g (MHz)
6.5×10^6	10^3-10^5	1.14	0.075 − 7.5	8.28 ± 1.24	1.12 ± 0.34

TABLE I. Q-factor values and dissipation rates for a Gd^{3+} spin-photon interaction at 14.9 GHz in frequency. Parameters of the model, including coupling (g) and concentration (n) were estimated from frequency and Q detuning models as shown in Fig. 5. The cooperativity of the interaction, $C = \frac{4g^2}{\Gamma_p\Gamma_s} > 590$, suggesting strong coupling according to the definition of $C > 1$.

of free space. Note, this assumes the concentration of spins is uniform, and really is the average concentration over the mode volume. With sufficient coupling rate, spin interactions such as those shown in Fig. 4 help derive spin quality factor (Q_s), g_L, and impurity concentrations. The frequency splitting of the perturbation in Fig. 4**A** at the magnetic field value where $\omega_s = \omega_p$ is equal to the magnitude of $2g/2\pi$ and secondary information such as Q_s and can be extracted by fitting Fig. 4**B** as per equation 3, with the results presented in Table I.

B. Impurity Identification, g_L, and ZFS

Multiple WGMs between 7 to 22 GHz were tracked simultaneously as the magnetic field strength was increased with a span of order 30 kHz, similar to that shown for the 14.9 GHz mode in Fig. 2. The Resulting mode-map of WGM-spin interactions is plotted in Fig. 6, and from this data, g_L and ZFS were extracted (see Tab. II). These two parameters take unique values for a paramagnetic impurity in a given host and are experimentally determined values. Thus, comparing observed g_L and ZFS values to previous investigations of doped $CaWO_4$ allowed for the identification of some of the paramagnetic impurities within this particular crystal.

The energy of the spin ensembles are modelled using a spin Hamiltonian that takes into consideration the following contributions; the Zeeman splitting term, the crystal field, and hyperfine splitting due to spin-orbit coupling. On the scale of GHz, spin-orbit coupling was not elucidated by the data, as the detuning resolution and the uncertainty of the detuning from the fitting is on the same order of magnitude as the hyper-fine structure constants. Thus, their contribution was neglected for the present study and our focus was to determine the crystal field zero-field splitting and the Zeeman splitting term. The Zeeman term gives us the value of g_L and we extract this value from the slopes of the Zeeman levels as a function of magnetic field. The crystal field parameters are constructed by well-defined tesseral harmonics that describe the spin energy levels. We choose the Stevens representation, which build operators from a spin operator basis, and determines the Stevens coefficients experimentally. Comparison between Fig. 6 data and Hamiltonian fits from prior literature that analysed doped $CaWO_4$ samples, served to check, corroborate or eliminate potential impurity species.

The scheelite unit cell comprises of two types of atom clusters, O-Ca and O-W. Whilst the the global symmetry is tetragonal, the Ca and W centered clusters present tetragonal and distorted hexagonal symmetries respectively, by the arrangement of surrounding oxygen. The tetragonal Ca cluster has symmetry isomorphic to S4 point symmetry [34] and is a likely occupation site for replacement by rare-earth and shell-3d transition metal impurities. Through the process of matching g_L, ZFS and other crystal field parameters we found that Fe^{3+} and Gd^{3+} were present in the sample, along with other unidentified trace rare-earth contaminants.

The crystal field of $CaWO_4$:Gd^{3+} was modelled in this work by the following Hamiltonian;

$$\begin{aligned}\mathcal{H} =\,& g_L\mu_B H_z S_z + B_2^0 O_2^0 + B_4^0 O_4^0 \\ &+ B_4^4 O_4^4 + B_6^0 O_6^0 + B_6^4 O_6^4\,,\end{aligned} \tag{5}$$

where O_k^j are Stevens operators, $S = \frac{7}{2}$ and $g_L = 1.99$. The crystal field parameters are; $B_2^0 = -9.215\cdot10^{-1}$, $B_4^0 = -1.139\cdot10^{-3}$, $B_4^4 = -7.015\cdot10^{-3}$, $B_6^0 = 5.935\cdot10^{-7}$, and $B_6^4 = 4.747\cdot10^{-7}$ in units of GHz. This Hamiltonian

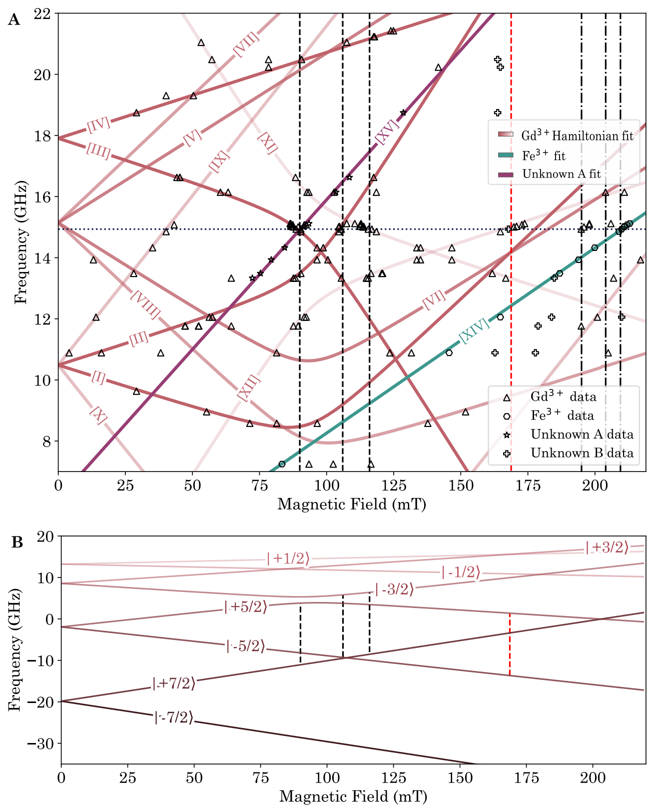

FIG. 6. **A** Shown are the perturbation sites in the frequency to magnetic field parameter space across the span of all WGMs employed. Spin transitions in $CaWO_4$:Gd^{3+} (orange) are derived from the spin Hamiltonian (see equation 5) and the corresponding transitions are shown in the $CaWO_4$:Gd^{3+} energy-level diagram in **B**. The horizontal, dotted, blue line marks the resonant frequency of the WGM shown in Fig. 4**D**. The vertical, dashed lines illustrate the link between magnetic field location, transition frequency, and perturbation effects in **A**, **B**, and Fig. 4,respectively. The Fe^{3+} transition is shown in green ($g_L = 4.3$, ZFS = 2.20 GHz) and another unidentified paramagnetic impurity species ($g_L = 7$, ZFS = 6.10 GHz) is shown in purple and denoted "Unkown A" data. Additional perturbations with no clear regression-line can be seen at higher field and are designated as "Unknown B" data. The vertical, black, dash-dotted lines correspond to the magnetic field locations of unidentified transition excited in Fig. 4 and belonging to Fe^{3+} and Unknown B.

allows the determination of the Zeeman energy levels of Gd^{3+} in $CaWO_4$, which are shown in Fig. 6**B**. Note, not all the energy levels are occupied or coupled to with the present setup, thus, not every energy level theoretically predicted is reflected in the experiment. The energy difference (vertical dashed lines) between the allowed transitions of these levels (coloured lines) allows one to identify the spin transitions in Fig. 6**A**. This result is in good agreement with the literature [35] with the only discrepancy being a 3.14% increase in the value of B_2^0 which dictates the ZFS values. This is due to the difference in orientation of this sample's c-axis to that of Baibekov

Species	ΔS_z	Line	ZFS (GHz)	Transition
$CaWO_4$:Gd^{3+} $g_L = 1.99$	1	I	4.61	$\lvert -3/2\rangle \rightarrow \lvert -1/2\rangle$
		II	10.42	$\lvert +5/2\rangle \rightarrow \lvert +3/2\rangle$
		III		$\lvert -5/2\rangle \rightarrow \lvert -3/2\rangle$
		IV	17.90	$\lvert +7/2\rangle \rightarrow \lvert +5/2\rangle$
		V		$\lvert -7/2\rangle \rightarrow \lvert -5/2\rangle$
	2	VI	15.03	$\lvert -5/2\rangle \rightarrow \lvert -1/2\rangle$
		VII		$\lvert +5/2\rangle \rightarrow \lvert +1/2\rangle$
	3	VIII	15.03	$\lvert -5/2\rangle \rightarrow \lvert +1/2\rangle$
		IX		$\lvert +5/2\rangle \rightarrow \lvert -1/2\rangle$
	4	X	10.42	$\lvert -5/2\rangle \rightarrow \lvert +3/2\rangle$
		XI		$\lvert +5/2\rangle \rightarrow \lvert -3/2\rangle$
	5	XII	2.22	$\lvert +7/2\rangle \rightarrow \lvert -3/2\rangle$
		XIII	28.33	$\lvert -5/2\rangle \rightarrow \lvert +5/2\rangle$
$CaWO_4$:Fe^{3+} $g_L = 4.3$	-	XIV	2.20	-
Unknown A $g_L = 7$	-	XV	6.10	-

TABLE II. Determined properties of some spin transitions calculated form the multi-mode spectroscopy. Here ΔS_z is the change in spin quantum number.

et.al. who use a $\langle 001\rangle$ cut single crystal. Gd^{3+} exhibits a distinctive electronic structure with the ground and first excited state are separated by a seven photon transition [36]. Occupation of states requiring a high photon number to transition to are less likely to occur. Hence, spin occupation is distributed to a greater number of excited states than would be expected at thermodynamic equilibrium when cooled to 30mK. Time series data verify that the tuning rate of the magnetic field was sufficiently slow to avoid reading transient and heating effects at the instance of data acquisition. The results presented here are consistent with the findings in [36] where this was indeed the case. To speculate at the source of this Gd^{3+} contamination, we note that the YVO_4 sample reported in [36] also had excess Gd^{3+} ions, and is purchased from this same manufacturer, and it may be that one of their production stations was contaminated with gadolinium. The coupling rates determined by the present study indicate it may be possible to achieve strong coupling. Accordingly, the presence of this dilute spin ensemble may be exploited in multiple avenues from bolometric sensing to qubit applications since the low concentration of spins, on the order of ppb, preserve the Q of the dielectric, whilst exhibiting sensitivity to photon coupling.

The Fe^{3+} ($g_L = 4.3$, ZFS = 2.20 GHz) transition was observed [37, 38]. Coupling to this species was too weak to fit to and hence determine the concentration. Another clear linear regression is present at low frequency and high magnetic field, denoted as unknown A. This unknown spin ensemble has low ZFS and high g_L factor, indicating that it may be a rare-earth species. Other residual perturbation sites, simply designated as "Unkown B" are shown with no clear trend or regression to allow identification. More data in this region of the perturbation map is need to elucidate these contributions to the spectra.

IV. CONCLUSION

This study found the presence of dilute spin ensembles in a scheelite sample, with Gd^{3+} being the dominant species. Fe^{3+} and another unknown species "A" are also shown in the ESR spectra at much lower concentrations. High-Q WGMs show that this material exhibits low-loss at mK temperatures of order 3×10^{-8} at 14 GHz in frequency. The high-Qs of the WGMs allowed us to perform highly sensitive multi-mode spectroscopy on the sample. This work has identified the of paramagnetic spin impurities in crystalline $CaWO_4$, useful for designs which require coherent spin ensembles to perform quantum information

ACKNOWLEDGEMENTS

This work was funded by the ARC Centre of Excellence for Engineered Quantum Systems, CE170100009, and Dark Matter Particle Physics, CE200100008. BM was also funded by the Forrest Research Foundation.

REFERENCES

[1] W. B. Mims. Phase memory in electron spin echoes, lattice relaxation effects in cawo$_4$: Er, ce, mn. *Phys. Rev.*, 168:370–389, Apr 1968.

[2] Bernal G. Enrique. Optical Spectrum and Magnetic Properties of Er3+ in CaWO4. *The Journal of Chemical Physics*, 55(5):2538–2549, 12 2003.

[3] S. Bertaina, S. Gambarelli, A. Tkachuk, I. N. Kurkin, B. Malkin, A. Stepanov, and B. Barbara. Rare-earth solid-state qubits. *Nature Nanotechnology*, 2(1):39–42, 2007.

[4] S. Bertaina, J. H. Shim, S. Gambarelli, B. Z. Malkin, and B. Barbara. Spin-orbit qubits of rare-earth-metal ions in axially symmetric crystal fields. *Phys. Rev. Lett.*, 103:226402, Nov 2009.

[5] S. Probst, G. Zhang, M. Rančić, V. Ranjan, M. Le Dantec, Z. Zhang, B. Albanese, A. Doll, R. B. Liu, J. Morton, T. Chanelière, P. Goldner, D. Vion, D. Esteve, and P. Bertet. Hyperfine spectroscopy in a quantum-limited spectrometer. *Magnetic Resonance*, 1(2):315–330, 2020.

[6] M. Rančić, M. Le Dantec, S. Lin, S. Bertaina, T. Chanelière, D. Serrano, P. Goldner, R. B. Liu, E. Flurin, D. Estève, D. Vion, and P. Bertet. Electron-spin spectral diffusion in an erbium doped crystal at millikelvin temperatures. *Phys. Rev. B*, 106:144412, Oct 2022.

[7] Marianne Le Dantec, Miloš Rančić, Sen Lin, Eric Billaud, Vishal Ranjan, Daniel Flanigan, Sylvain Bertaina, Thierry Chanelière, Philippe Goldner, Andreas Erb, Ren Bao Liu, Daniel Estève, Denis Vion, Emmanuel Flurin, and Patrice Bertet. Twenty-three–millisecond electron spin coherence of erbium ions in a natural-abundance crystal. *Science Advances*, 7(51):eabj9786, 2021.

[8] Salim Ourari, Łukasz Dusanowski, Sebastian P. Horvath, Mehmet T. Uysal, Christopher M. Phenicie, Paul Stevenson, Mouktik Raha, Songtao Chen, Robert J. Cava, Nathalie P. de Leon, and Jeff D. Thompson. Indistinguishable telecom band photons from a single er ion in the solid state. *Nature*, 620(7976):977–981, 2023.

[9] R. M. Rakhmatullin, I. N. Kurkin, G. V. Mamin, S. B. Orlinskii, M. R. Gafurov, E. I. Baibekov, B. Z. Malkin, S. Gambarelli, S. Bertaina, and B. Barbara. Coherent spin manipulations in yb^{3+} : cawo$_4$ at x- and w-band epr frequencies. *Phys. Rev. B*, 79:172408, May 2009.

[10] C. G. B. Garrett and F. R. Merritt. PMR SPECTRA OF Nd3+ IN COMPENSATED AND UNCOMPENSATED CaWO4. *Applied Physics Letters*, 4(2):31–32, 12 2004.

[11] I. B. Aizenberg, F. Z. Gil'fanov, and A. L. Stolov. Absorption and luminescence spectra of pr^{3+} in cawo4 monocrystals. *Soviet Physics Journal*, 9(1):29–33, 1966.

[12] Enrico Cavalli, Philippe Boutinaud, and Marek Grinberg. Luminescence dynamics in cawo4:pr3+ powders and single crystals. *Journal of Luminescence*, 169:450–453, 2016. The 17th International Conference on Luminescence and Optical Spectroscopy of Condensed Matter (ICL'14).

[13] Tian-Shu Yang, Ming-Xu Su, Jian-Yin Huang, You-Cai Lv, Zong-Quan Zhou, Chuan-Feng Li, and Guang-Can Guo. Spectroscopic investigations of pr^{3+} : cawo$_4$ at liquid-helium temperatures. *Phys. Rev. A*, 107:022802, Feb 2023.

[14] Giovanni Franco-Rivera, Josiah Cochran, Seiji Miyashita, Sylvain Bertaina, and Irinel Chiorescu. Strong coupling of a Gd^{3+} multilevel spin system to an on-chip superconducting resonator. *Phys. Rev. Appl.*, 19:024067, Feb 2023.

[15] G. Franco-Rivera, J. Cochran, L. Chen, S. Bertaina, and I. Chiorescu. On-chip detection of electronuclear transitions in the ^{155,157}Gd multilevel spin system. *Phys. Rev. Appl.*, 18:014054, Jul 2022.

[16] Yu.G. Zdesenko, F.T. Avignone, V.B. Brudanin, F.A. Danevich, V.V. Kobychev, B.N. Kropivyansky, S.S. Nagorny, V.I. Tretyak, and Ts. Vylov. Carvel experiment with $^{48}cawo_4$ crystal scintillators for the double β decay study of ^{48}ca. *Astroparticle Physics*, 23:249–263, 2005.

[17] C. Cozzini, G. Angloher, C. Bucci, F. von Feilitzsch, D. Hauff, S. Henry, Th. Jagemann, J. Jochum, H. Kraus, B. Majorovits, V. Mikhailik, J. Ninkovic, F. Petricca, W. Potzel, F. Pröbst, Y. Ramachers, W. Rau, M. Razeti, W. Seidel, M. Stark, L. Stodolsky, A. J. B. Tolhurst, W. Westphal, and H. Wulandari. Detection of the natural α decay of tungsten. *Phys. Rev. C*, 70:064606, Dec

2004.
[18] G. Angloher, C. Bucci, P. Christ, C. Cozzini, F. von Feilitzsch, D. Hauff, S. Henry, Th. Jagemann, J. Jochum, H. Kraus, B. Majorovits, J. Ninkovic, F. Petricca, W. Potzel, F. Pröbst, Y. Ramachers, M. Razeti, W. Rau, W. Seidel, M. Stark, L. Stodolsky, A.J.B. Tolhurst, W. Westphal, and H. Wulandari. Limits on wimp dark matter using scintillating cawo4 cryogenic detectors with active background suppression. *Astroparticle Physics*, 23:325–339, 2005.
[19] M.v. Sivers, C. Ciemniak, A. Erb, F.v. Feilitzsch, A. Gütlein, J.-C. Lanfranchi, J. Lepelmeier, A. Münster, W. Potzel, S. Roth, R. Strauss, U. Thalhammer, S. Wawoczny, M. Willers, and A. Zöller. Influence of annealing on the optical and scintillation properties of cawo4 single crystals. *Optical Materials*, 34(11):1843–1848, 2012.
[20] Warrick G. Farr, Daniel L. Creedon, Maxim Goryachev, Karim Benmessai, and Michael E. Tobar. Ultrasensitive microwave spectroscopy of paramagnetic impurities in sapphire crystals at millikelvin temperatures. *Phys. Rev. B*, 88:224426, Dec 2013.
[21] Rouaida Abozaid, Zorica Lazarevic, Vesna Radojevic, Maja Rabasovic, Dragutin Sevic, Mihailo Rabasovic, and Nebojsa Romcevic. Characterization of neodymium doped calcium tungstate single crystal by raman, ir and luminescence spectroscopy. *Science of Sintering*, 50:445–455, 01 2018.
[22] *Dielectric resonators.* 1986.
[23] Mikhail F. Limonov, Mikhail V. Rybin, Alexander N. Poddubny, and Yuri S. Kivshar. Fano resonances in photonics. *Nature Photonics*, 11(9):543–554, Sep 2017.
[24] Michael Edmund Tobar, Jerzy Krupka, Eugene Nicolay Ivanov, and Richard Alex Woode. Anisotropic complex permittivity measurements of mono-crystalline rutile between 10 and 300 k. *Journal of Applied Physics*, 83(3):1604–1609, 1998.
[25] J. Krupka, K. Derzakowski, A. Abramowicz, M. E. Tobar, and R. G. Geyer. Use of whispering-gallery modes for complex permittivity determinations of ultra-low-loss dielectric materials. *IEEE Transactions on Microwave Theory and Techniques*, 47(6):752–759, 1999.
[26] Jerzy Krupka, Krzysztof Derzakowski, Michael Tobar, John Hartnett, and Richard G Geyer. Complex permittivity of some ultralow loss dielectric crystals at cryogenic temperatures. *Measurement Science and Technology*, 10(5):387, 1999.
[27] Warrick G Farr, Daniel L Creedon, Maxim Goryachev, Karim Benmessai, and Michael E Tobar. Ultrasensitive microwave spectroscopy of paramagnetic impurities in sapphire crystals at millikelvin temperatures. *Physical Review B*, 88(22):224426, 2013.
[28] Eisuke Abe, Hua Wu, Arzhang Ardavan, and John J. L. Morton. Electron spin ensemble strongly coupled to a three-dimensional microwave cavity. *Applied Physics Letters*, 98(25):251108, 06 2011.
[29] K. Sandner, H. Ritsch, R. Amsüss, Ch. Koller, T. Nöbauer, S. Putz, J. Schmiedmayer, and J. Majer. Strong magnetic coupling of an inhomogeneous nitrogen-vacancy ensemble to a cavity. *Phys. Rev. A*, 85:053806, May 2012.
[30] M.E. Tobar and D.G. Blair. A generalized equivalent circuit applied to a tunable sapphire-loaded superconducting cavity. *IEEE Transactions on Microwave Theory and Techniques*, 39(9):1582–1594, 1991.
[31] N. C. Carvalho, M. Goryachev, J. Krupka, P. Bushev, and M. E. Tobar. Low-temperature microwave properties of biaxial yalo$_3$. *Phys. Rev. B*, 96:045141, Jul 2017.
[32] Michael E. Tobar. *Gravitational Wave Detection and Low-Noise Sapphire Oscillators.* PhD thesis, The University of Western Australia, arXiv:2311.16426 [gr-qc], 1994.
[33] Jeremy F. Bourhill. *Quantum Hybrid Systems in Low-Loss Crystalline Solids.* PhD thesis, The University of Western Australia, 2016.
[34] M.V. Nazarov, B.S. Tsukerblat, E.-J. Popovici, and D.Y. Jeon. Optical lines in europium–terbium double activated calcium tungstate phosphor. *Physics Letters A*, 330(3):291–298, 2004.
[35] E. I. Baibekov, M. R. Gafurov, D. G. Zverev, I. N. Kurkin, A. A. Rodionov, B. Z. Malkin, and B. Barbara. Coherent spin dynamics in a gadolinium-doped cawo4 crystal. *Physical Review B*, 95(6), feb 2017.
[36] Lingfei Zhao, Maxim Goryachev, Jeremy Bourhill, and Michael Tobar. Indirect methods to control population distribution in a large spin system. *New Journal of Physics*, 19, 03 2017.
[37] R Golding, M Kestigian, and William Tennant. Epr of high-spin fe3+ in calcium tungstate, cawo4. *Journal of Physics C: Solid State Physics*, 11:5041, 02 2001.
[38] D.G McGavin and W.C Tennant. Epr study of high-spin ferric ion in a completely rhombic environment. fe3+ in cawo4. *Journal of Magnetic Resonance (1969)*, 61(2):321–332, 1985.

V. APPENDIX

In this appendix we show 26 density plots (Fig.7) for many photon-sipn mode interactions, with some plotted in Fig.6 in the main body of the paper.

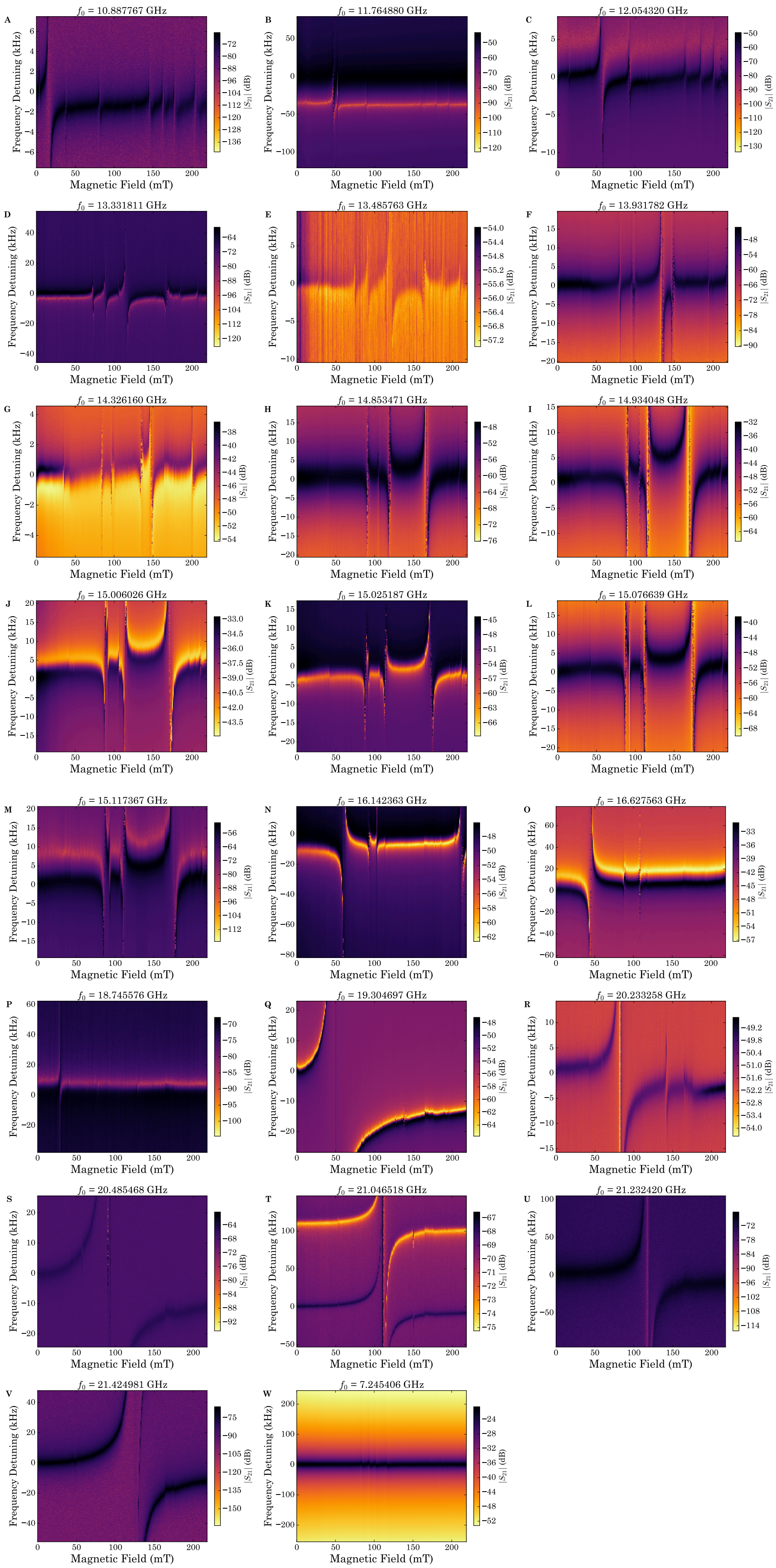

FIG. 7. Density plots (A-W) of resonator transmission power using the setup in Fig.2